Structure and microstructure of $La_{1-x}Ca_xMnO_{3-\delta}$ thin films prepared by pulsed laser deposition

O. I. Lebedev
EMAT, University of Antwerp (RUCA), Groenenborgerlaan 171, B-2020 Antwerp, Belgium and Max-Planck-Institut für Festkörperforschung, D-70506 Stuttgart, Germany

G. Van Tendeloo* and S. Amelinckx
EMAT, University of Antwerp (RUCA), Groenenborgerlaan 171, B-2020 Antwerp, Belgium

B. Leibold and H.-U. Habermeier
Max-Planck-Institut für Festkörperforschung, D-70506 Stuttgart, Germany

(Received 29 December 1997)

$La_{1-x}Ca_xMnO_{3-\delta}$ (LCMO) thin films are grown by pulsed laser deposition on a (100) $SrTiO_3$ substrate at temperatures between 530 and 890 °C. The magnetotransport properties show a high negative magnetoresistance and a shift of the maximum of the $R(T)$ curve as a function of temperature. The Curie temperature changes with deposition temperature and film quality in the range of 100–220 K. The film quality is characterized by x-ray diffraction and transmission electron microscopy (TEM); film and target compositions were verified by atomic emission spectroscopy. The local structure of the film depends on the growth conditions and substrate temperature. TEM reveals a slight distortion of the film possibly leading to a breakdown of the symmetry from orthorhombic to monoclinic. At the highest growth temperatures, a well-defined interface is observed within the LCMO film, parallel to the substrate surface; this interface divides the film into two lamellae with a different microstructure. The one close to the substrate is perfectly coherent with the substrate, suggesting that it is strained as a result of the lattice parameter mismatch; the upper lamella shows a typical domain structure with unusual translation interfaces characterized by a displacement vector of the type $\frac{1}{2}[101]_o$ and $\frac{1}{2}[101]_o$ when referred to the orthorhombic lattice.
[S0163-1829(98)01836-0]

I. INTRODUCTION

The magnetic and electronic properties of alkaline earth substituted perovskite-type manganese oxides of the general formula $A_{1-x}B_xMnO_{3-\delta}$ with $A=$La, Pr, Nd, and $B=$Ca, Sr, Ba have recently attracted considerable interest.[1–5] From the fundamental point of view these compounds show a wide variety of interesting physical phenomena due to the strong tendency to undergo structural instabilities inherent to all transition metal perovskite oxides. These instabilities are related to either ferroelectricity or antiferroelectricity and to various kinds of magnetic ordering. The electronic transport properties are especially of interest; in particular the magnetic field driven shift of the metal-insulator transition leading to a colossal negative magnetoresistance (CMR) $[\Delta R/R(H)>10^{11}\%]$ (Ref. 6) is of fundamental as well as of potential technological importance.

At present it is well established that the structure of the CMR perovskite strongly influences the physical properties. However, the complicated structure of $A_{1-x}B_xMnO_{3-\delta}$ involves many parameters and it is not so clear how these parameters influence the CMR properties. In the literature it is, for instance, well documented that the structural, magnetic, and magnetotransport properties depend on the composition at a microscopic level, on the growth conditions, on the oxidation state, on the epitaxy in the case of thin layers, and on the overall microstructure.[9]

The CMR oxides have a (001) layerlike perovskite-type structure with ferromagnetic ordering in the MnO layers and a doping-dependent antiferromagnetic $[x<0.2$ and $x>0.5]$ or ferromagnetic $[0.2<x<0.5]$ ordering along the layer normal. The perovskitelike structure is very prone to subtle structural transformations as well as to lattice distortions. These distortions depend on the nature of the cations and on the oxygen stoichiometry. Manganese perovskites potentially offer large possibilities due to the ability of Mn to take the two oxidation states Mn^{+3} and Mn^{+4}; the latter ion having the smaller ionic radius. A linear decrease of the lattice parameter with increasing Ca contents and a change of the structure from tetragonal to cubic with increasing Ca contents have been reported.[7–9] A monoclinic distortion has also been reported by several authors.[10,11] All these distorted structures are very similar; in one case the presence of two different distortions has been assumed.[11] A drastic decrease of the b_o and an increase of the a_o and c_o parameters, due to Jahn-Teller distortion of the MnO_6 octahedra, was found in the orthorhombic phase.[13,14] The importance of the Jahn-Teller lattice distortion was demonstrated by a giant oxygen isotope shift in $La_{1-x}Ca_xMnO_{3-\delta}$.[15]

Since the CMR effect has been observed in thin films of $La_{1-x}Ca_xMnO_{3-\delta}$ (Ref. 16) the main interest was focused on the compound with $x\approx0.3$. It was proposed that such a large change in magnetoresistivity is due to the defect structure in epitaxially grown films. In thin films deviations from the cubic structure can become more pronounced due to the influence of the substrate and as a result of the larger possibilities for atomic rearrangements as a result of diffusion during the film deposition. Not only possible strain between the film

and the substrate induced by lattice mismatch may cause possible distortions but also the quality of the substrate surface is important in this respect. The structure of thin film $La_{1-x}Ca_xMnO_{3-\delta}$ with $x=0.3-0.35$ is most commonly described as a cubic perovskitetype structure or as a tetragonally distorted perovskite structure.[16–18]

The microstructural changes are usually too small to lead to observable splitting of x-ray reflections. In this respect transmission electron microscopy (TEM) and, in particular, high-resolution electron microscopy (HREM) may be the more sensitive probes.

II. EXPERIMENTAL METHODS

A. Preparation of films

$La_{1-x}Ca_xMnO_{3-\delta}$ (LCMO) thin films were deposited on a $SrTiO_3$ [strontium titanite (STO)] single crystal by pulsed laser deposition (PLD) using a ceramic disk-shaped target. An excimer laser filled with a KrF gas mixture emitting UV radiation at a wavelength $\lambda=248$ nm was the energy source. The pulse duration was 28 ns. Similar setups were used previously to prepare Y-Ba-Cu-O thin films.[19] The ceramic target contained cation atoms in the nominal ratio La-Ca:Mn $=2:1:3$; it was prepared by the standard solid-state reaction using oxidic precursors. Films with a thickness of 250 nm were grown with the substrate heated to temperatures in the range from 530 to 890 °C under 50 Pa of flowing oxygen. Immediately after deposition the films were subjected to an *in situ* annealing step at 750 °C during 1 h at ambient oxygen pressure and subsequently cooled to room temperature. The films grown at 530, 720, and 890 °C were examined in detail by a variety of methods. Also, a few very thin films were produced in order to be able to examine the initial growth stages.

B. Specimen preparation

Specimens for transmission electron microscope studies were prepared by ion milling. Two types of specimens were prepared: plan-view and cross-section specimens.

Plan-view specimens were made parallel to the (100) STO plane by thinning from the substrate side. They were first grinded mechanically to a thickness of about 90 μm, followed by dimpling in a Gatan dimpler. The final ion-beam milling was done by Ar^+ bombardment at 4 KeV in a Balzers REP 010 equipment. The guns were oriented under a grazing incidence angle of about 8° with respect to the surface, each gun carrying a current of 1 mA. The specimen was further oscillated in azimuth over an angle of 40° during the ion-beam milling.

Cross-section specimens were prepared parallel to the (010) or (001) plane of STO, using similar thinning methods. Plan view specimens free of the substrate could be obtained, cross-section specimens always contain areas both of the LCMO phase and of the STO substrate.

III. EXPERIMENTAL METHODS AND RESULTS

A. Chemical composition

The chemical compositions of the deposited film and of the target were determined, after dissolution, by atomic emission spectroscopy using an inductively coupled plasma (AES-ICP) as a light source. This method allows a high precision for the determination of the cation ratios. The composition of the film was found to correspond within the experimental error to that of the target i.e., $x=0.3$.

TABLE I. Structure and magnetotransport data.

T_s (°C)	Thickness (nm)	a_p (nm)	T_{Curie} (K)	$(\text{DR/RH})_{\max}$, %	AES-ICP La/Ca/Mn
		0.3874			
530	250	0.3880	100	730	0.71/0.34/1.0
		0.3878			
720	260	0.3868	163	2190	0.70/0.34/1.0
890	250	0.3836	220	1282	0.69/0.35/1

B. Phase analysis

X-ray diffraction of the composite sample substrate and film revealed the presence of a single-phase textured LCMO film in parallel epitaxial relationship with the substrate, for a wide range of substrate temperatures. However, the films deposited at 530 °C or lower produced a diffractogram exhibiting two extra peaks, which points to the presence of a second phase with lattice parameters close to those of the main phase. The diffractogram can roughly be indexed on the basis of a cubic lattice with a lattice parameter $a_p=0.38$ nm, which is compatible with a perovskite-type structure. However, taking into account the crystallographic data for bulk material, with composition $x=0.3$, the x-ray diffraction pattern was indexed on an orthorhombic lattice with parameters $a\approx c=0.5451$ nm ($\approx a_p\sqrt{2}$) and $b=0.7678$ nm ($\approx 2a_p$) and with space group *Pnma* leading to diffraction conditions: $okl\ k+l=2n$; $hko\ h=2n$; $oko\ k=2n$; $hoo\ h=2n$; $ool\ l=2n$.

C. Colossal magnetoresistance measurement

All considered films exhibit significant magnetotransport properties as summarized in Table I. The figure of merit $(\Delta R/R_H)_{\max}$ seems to improve with increasing temperature of the substrate during deposition. In particular, the Curie temperature increases with increasing deposition temperature and correspondingly the structure of the films becomes more perfect.

D. Electron microscopy

Electron diffraction patterns and high-resolution images were obtained using a Jeol 4000FX and a Jeol 4000EX microscope; both instruments were operated at 400 kV. The resolution of the microscopes is of the order of 0.2 and 0.16 nm, respectively. The image simulations of proposed structure models were carried out with the EMS program and Mac Tempas software. For the basic structure simulation different specimen thicknesses in the range from 1.5 to 9.3 nm and defocus values in the range from -20 to -70 nm were assumed. The computed images were compared with the observed HREM images. For the simulation of the domain

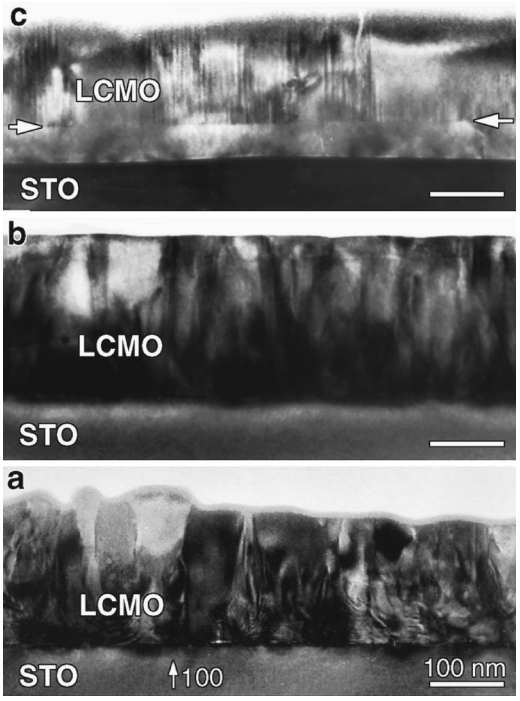

FIG. 1. Low magnification multibeam bright field diffraction contrast image of the columnar texture of (La, Ca)MnO_3 film deposited at different substrate temperatures: (a) 530 °C, (b) 720 °C, (c) 890 °C. The substrate is STO limited by a cube plane. Note that in (c) a perfectly epitaxial transition layer has been formed.

boundaries the periodic continuation method was applied to a crystal block containing a model of the antiphase boundary.

Multibeam bright field diffraction contrast images allow to obtain an overview of the microstructure of the film. The cross section images of Fig. 1 illustrate the dependence of the microstructure on the substrate temperature T_S.

At low substrate temperature ($T_S \sim 530$ °C) the film has a grainy microstructure with a large number of defects visualized as dark areas. The average grain size is about 40–100 nm. The contact plane between film and substrate is rough. At higher temperature (720 °C) the grain size is larger and the film acquires a domain structure consisting of columns, elongated along the substrate normal, and separated by interfaces. The contact surface between film and interface becomes smoother, and dark areas, revealing faults and strains, are no longer visible.

At the highest temperature ($T_S \sim 890$ °C) the film-substrate interface becomes flat and sharp and a perfectly monocrystalline layer with a thickness of about 100 nm, separating the substrate from the columnar structure, is formed. In plan view specimens the columns are visible as small domains surrounded by bright lines, which will be shown below to be the images of anti-phase boundaries (Fig. 2).

The very thin films grown under the same conditions as previously described exhibit an island structure (Fig. 3): the coverage of the substrate being only partial.

IV. INTERPRETATION

A. Electron diffraction patterns

Diffraction patterns of the LCMO layer can be obtained from plan-view specimens grown at 890 °C; such a pattern

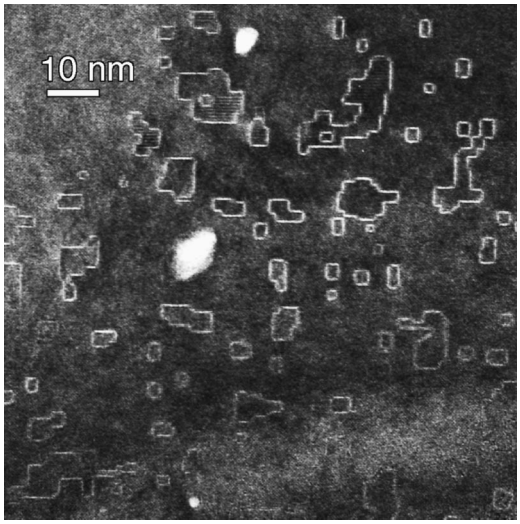

FIG. 2. Low magnification plan-view image of the prismatic antiphase boundaries a film deposited at 890 °C substrate temperature.

made with the beam parallel to the substrate normal is shown in Fig. 4(a). The indexing refers to an orthorhombic unit cell (space group *Pnma*). The pattern reflects the pseudofourfold symmetry along this zone. A diffraction pattern made of a cross section of the same specimen with the incident beam parallel to a cube direction of the substrate, parallel to the foil surface is shown in Fig. 4(b). Such patterns are the superposition of the patterns produced by the substrate and by the film.

In Fig. 5 the higher-order spots in the row $[oko]_o \equiv [hoo]_m$ are weakly split. The spots of the doublets that are closest to the origin of reciprocal space must be attributed to the film. The splitting thus shows that the lattice parameter along the substrate normal is slightly larger for the film than for the substrate. The spots along the rows parallel to the substrate are are very weakly split, the splitting only being visible in the high-order spots. This suggest a rather perfect match of the film and the substrate and the strained grown film (Fig. 6). Annealing of the sandwich produced widely separated interfacial dislocations, confirming the small misfit.

In a cubic crystal the pattern of the most intense spots would be perfectly square in both sections shown in Fig.

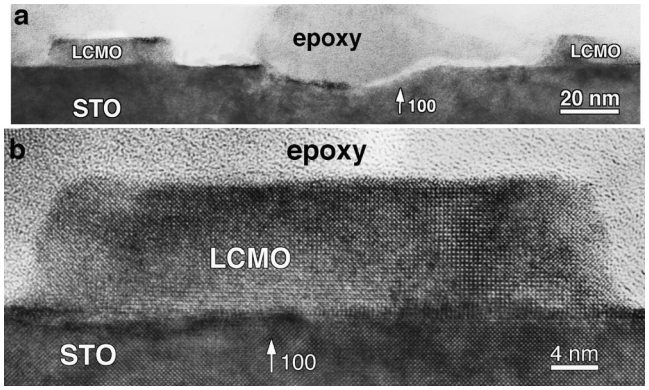

FIG. 3. Cross-section low magnification (a) overview and HREM image of islands in a very thin discontinuons (La, Ca)MnO_3 thin film consisting of separate islands.

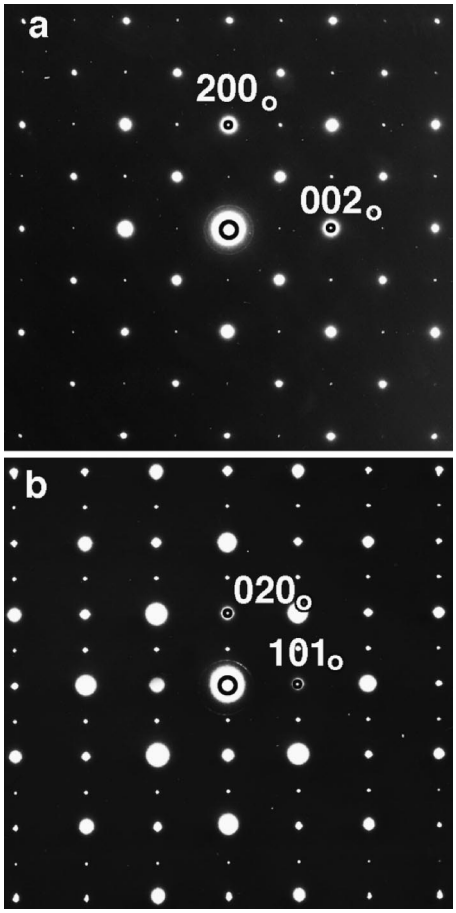

FIG. 4. Diffraction patterns of $(La, Ca)MnO_3$ along two relevant zones: (a) $[100]_m \equiv [010]_o$; (b) $[011]_m \equiv [101]_o$. In the diffraction pattern of (b) film as well as substrate contribute.

4(b). In actual fact it is found that the lattice is not cubic but to a good approximation orthorhombic since $g_{020,o} \geqslant g_{101,o}$. The angle between $g_{020,o}$ and $g_{101,o}$ is within experimental error 90°, but high-resolution images to be discussed below show a monoclinic angle β locally somewhat differing from

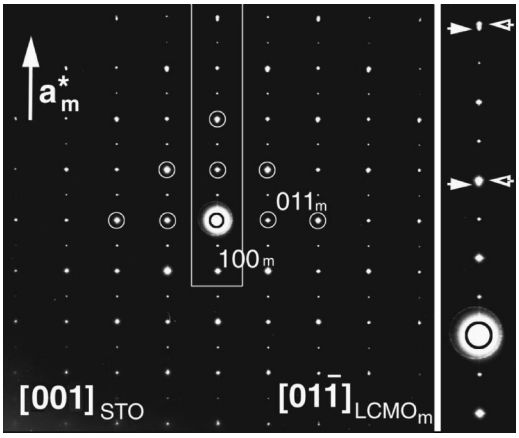

FIG. 5. Diffraction pattern of a selected area of a cross-section specimen containing film and substrate areas. The pattern is the superposition of two patterns. The high-order hoo_m spots are visibly split due to the small difference in the lattice parameters of LCMO and STO.

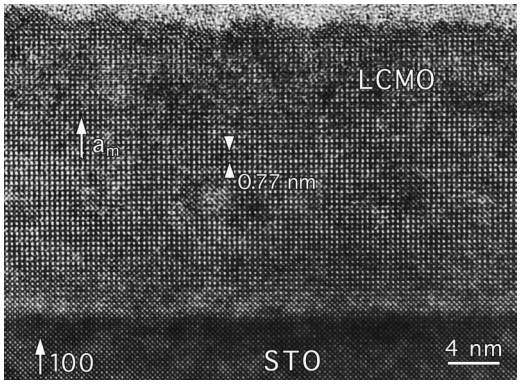

FIG. 6. Cross-section view along $[101]_o$ of perfect film of LCMO on a STO substrate. Note the dislocation free lattice match along the interface. The LCMO layer exhibits period doubling along the a_m direction.

90°. It is thus perhaps more appropriate to index this DP with reference to a monoclinic lattice. This has been done in Fig. 5.

The monoclinic deformation of the pattern of Fig. 4 is small enough to allow the superposition of the patterns of Figs. 4(a) and 4(b) without causing a visible splitting of the main spots. This is consistent with the appearance of patterns such as Figs. 7(a) and 7(b), which refers to a selected area covering two orientation variants of which the patterns of prominent spots differ by 45°. It shows that the specimen is fragmented in domains such that $[100]_{m,1}$ of variant 1 is parallel to $[011]_{m,2}$ of variant 2.

The electron diffraction patterns of a single domain (Fig. 4) can be indexed with reference to an orthorhombic lattice in which the direction normal to the substrate film interface is called $[010]_o$ with $b_o \approx 7.6$ Å and in which the direction $[100]_o$ with $a_o \approx 5.4$ Å and $[001]_o$ with $c_o \approx 5.4$ Å are parallel to this interface. In this approximation the lattice is tetragonal. In actual fact our x-ray diffraction data, which, in principle, allow a higher precision as to the measurement of the magnitude of lattice parameters, do not lead to an observable difference between a_o and c_o for thin films (See Table I). Moreover, we shall present further evidence that the lattice is in fact better described as slightly monoclinic (pseudo-orthorhombic).

With reference to the orthorhombic description the following diffraction conditions are found to be satisfied: *okl*, $k+l=2n$; *hoo*, $h=2n$; *hko*, $h=2n$; *ool*, $l=2n$.

The reflections *oko* are present for all integer values of *k*. This is not consistent with the diffraction conditions of the generally assumed *Pnma* spacegroup since this would, moreover, require *oko*, $k=2n$. Moreover, the HREM images of the film along the $[010]_o$ direction (Fig. 6) shows a clear doubling periodicity in one $[MnO]_2$ layer out of two.

On tilting the specimen about an axis parallel to the [010] zone the reflections with $k=2n+1$ in the pattern of Fig. 4 become very weak; they disappear almost completely if no intense spots are present capable of causing by double diffraction the appearance of intensity at $k=2n+1$ positions. This shows that the diffraction conditions for *Pnma* are only weakly ''frustrated'' suggesting that the real symmetry is lower. The actual space group is thus most probably a maximal subgroup of *Pnma*, which has to satisfy the above-

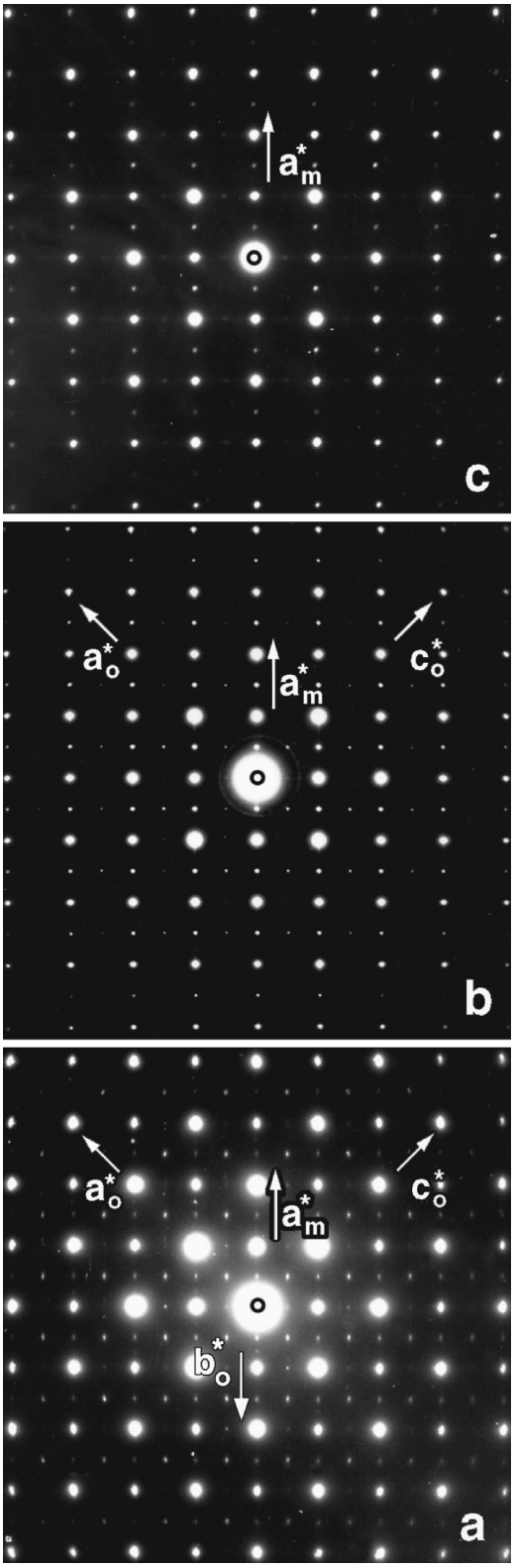

FIG. 7. Diffraction patterns along the same $[101]_o$ type zone, of three different specimens obtained at different temperatures of the substrate: (a) 530 °C three different domain orientations are present; (b) 720 °C two different domain orientations are present; (c) 890 °C single variant within the selected area.

mentioned diffraction conditions and, moreover, has to allow for the appearance of nonvanishing reflections with $k=2n+1$.

In Ref. 12 the spacegroup $P2_1/c$ was proposed for isotypic compounds such as $Pr_{0,7}Ca_{0,25}Sr_{0,05}MnO_3$ and $Pr_{0,75}Sr_{0,25}MnO_3$. We will show that also in the present case the diffraction patterns and the observed images suggest this space group and are difficult to account for in detail by assuming the space group to be *Pnma*.

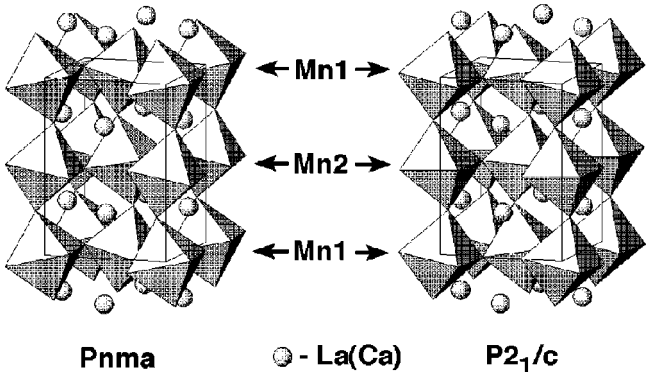

FIG. 8. Comparison of proposed unit cell of (La, Ca)MnO_3 based on two space groups *Pnma* and $P2_1/c$. The MnO_2 layers are marked by arrows.

Structure models based on *Pnma* and on $P2_1/c$ are compared in Fig. 8. In *Pnma* all MnO_6 octahedra remain essentially undeformed and the tilts are coupled by vertex sharing. In $P2_1/c$ on the other hand layers of MnO_6 octahedra parallel to $(010)_o$ are alternatingly undeformed, tilted by vertex sharing, and deformed by shearing. In this way the (010) family of glide mirror planes, which related these successive layers in *Pnma*, is eliminated.

Unfortunately it is not easy to obtain a single domain diffraction pattern; most diffraction patterns are in fact the superposition of two or three differently oriented patterns. This is, for instance, the case in Fig. 7. It is clear that (b) is obtained by the superposition of two patterns similar to (c) but differing by 45° in orientation. In Fig. 7(a) even a third variant differing 90° in orientation with that in (c) is superposed. These patterns were obtained from the three different samples shown in Fig. 1. It turns out that the number of orientation variants within the same size selected area is largest for the lowest substrate temperature; possibly because at the lower temperature the crystal structure is closer to cubic, but more important because the atom mobility is smaller.

Similar diffraction patterns were found by the authors of Ref. 12 where it was shown that bulk material exhibits a similar domain fragmentation, the density of domain boundaries being determined by the composition and the annealing temperature.

B. High-resolution microscopy

1. Cross-section specimens

Cross-section samples show the presence of a columnar type of growth (see Fig. 1) for different substrate temperatures. The HREM images mostly exhibit two different easily recognizable types of columns as judged by their difference in high-resolution image characteristics (Fig. 9). Columns exhibiting prominently a 0.38-nm-square bright dot pattern alternate with columns showing prominently a finer 0.27-nm-square bright dot pattern that results from centering of

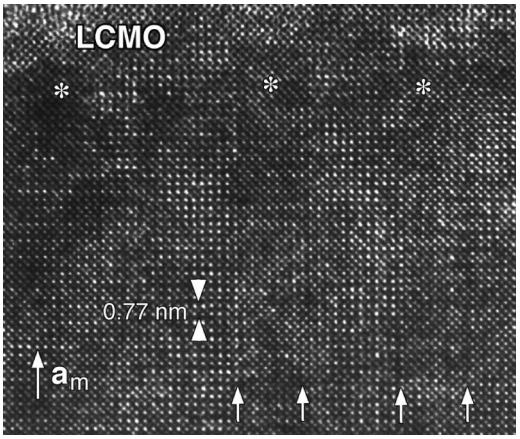

FIG. 9. High-resolution image of a cross-section specimen viewed along a $[101]_o$-type zone. Note the difference in image characteristics of neighboring columns, that are separated by planar interfaces.

the previous one. In a cross-section pattern the interfaces between two such columns are rather planar and imaged edge on. The image characteristics, however, sensitively depend on the specimen thickness and at the thinnest edges of the specimen the 0.27-nm pattern is observed in all columns.

It seems at first reasonable to attribute the domain structure to at least the two orientation variants of the structure with a common b_o axis. In the orthorhombic description these variants would result from an interchange of a_o and c_o, the contact plane being a $(101)_o$-type plane.

Such a domain structure is justified by symmetry considerations; taking into account, on the one hand, the pseudofourfold symmetry about the normal b_o of the substrate interface and the epitaxial relationship of the first LCMO layers and, on the other hand, the twofold rotation symmetry about the same axis of the pseudo-orthorhombic LCMO film structure. Two structural variants related by a 90° rotation about the b_o axis are thus to be expected.

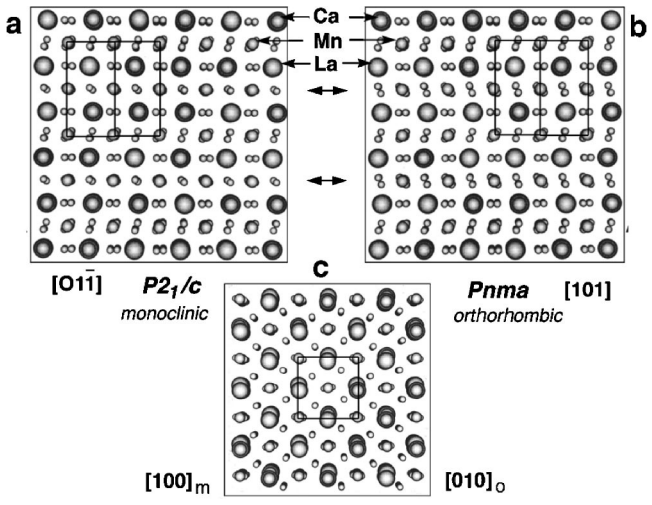

FIG. 10. Comparison of proposed structures of (La, Ca)MnO_3 based on two different space groups. (a) $[01\bar{1}]_m$ zone view of the monoclinic structure ($P2_1/c$), (b) $[101]_o$ zone view of the orthorhombic structure (*Pnma*), (c) common view of the two structures along the zones $[100]_m \equiv [010]_o$.

TABLE II. Positional parameters for $La_{0.7}Ca_{0.3}MnO_{3-\delta}$ (space group: *Pnma*).

Atom	x/a	y/b	z/c	Occup.
La	0.5436	0.25	0.0064	0.7
Ca	0.5436	0.25	0.0064	0.3
Mn	0	0	0	1
O(1)	−0.0108	0.25	−0.0734	1
O(2)	0.3015	0.0385	0.2258	1

In those regions where the image consists of the 0.38-nm-square dot pattern the period along the b_o axis is in many areas visibly doubled, i.e., equal to 0.77 nm. Weaker indications of period doubling are also sometimes discernable in the columns exhibiting the 2.7 Å square grid. The period doubling suggests that successive layers of MnO_6 octahedra along b_o (a_m) have a different geometry in projection along two viewing directions $[101]_o$ and $[\bar{1}01]_o$.

In the *Pnma* space-group-based structure such projections, of successive layers are identical. However, this is no longer the case in the $P2_1/c$-based structure because of the shearlike deformation of alternating layers (Fig. 10). The fractional atomic coordinates are summarized in Tables II and III for both space groups. The monoclinic distortion is simulated by slightly varying the coordinate of the O(2)′ atom marked by an asterisk from $x/a=0.4615$ to $x/a=0.5$.

The observed period doubling along $[010]_o \equiv [100]_m$ is apparently due to the fact that successive MnO_2 layers are imaged as rows of dots with a different ''grayness.'' This can be deduced from simulated images (Fig. 11). It should be noted that whereas manganese columns are imaged as the brightest dots and (La, Ca) as gray dots, in plan-view specimens such as Fig. 12 the reverse is true under the imaging conditions used on the cross-section specimen such as Fig. 6 and 13. This conclusion was reached, in the usual way by superposing the origins in the simulated images and in the projected model.

When using a model based on the *Pnma* space group the simulated pattern of the cross-section images shows the manganese layers in a darker contrast, but it fails to reveal a period doubling along $[010]_o$. This feature is correctly reproduced when a model is used based on a space group of lower symmetry, such as $P2_1/c$, which leads to successive MnO_2 layers having different projected structures. In Fig. 13 a simulated image, calculated for a

TABLE III. Positional parameters for $La_{0.7}Ca_{0.3}MnO_{3-\delta}$ (space group $P2_1/c$), $a_m=b_o=0.7672$ nm, $b_m=c_o=0.5447$ nm, $c_m=a_o=0.5453$ nm, $b=90.0°-90.3°$.

Atom	x/a	y/b	z/c	Occup.
La	0.25	0.0064	0.5436	0.7
Ca	0.25	0.0064	0.5436	0.3
Mn	0	0	0	1
Mn	0.5	0.5	0	1
O(1)	0.25	−0.0734	−0.0108	1
O(2)	0.0385	0.2258	0.3015	1
O(2)′	0.4615*	0.2258	0.3015	1

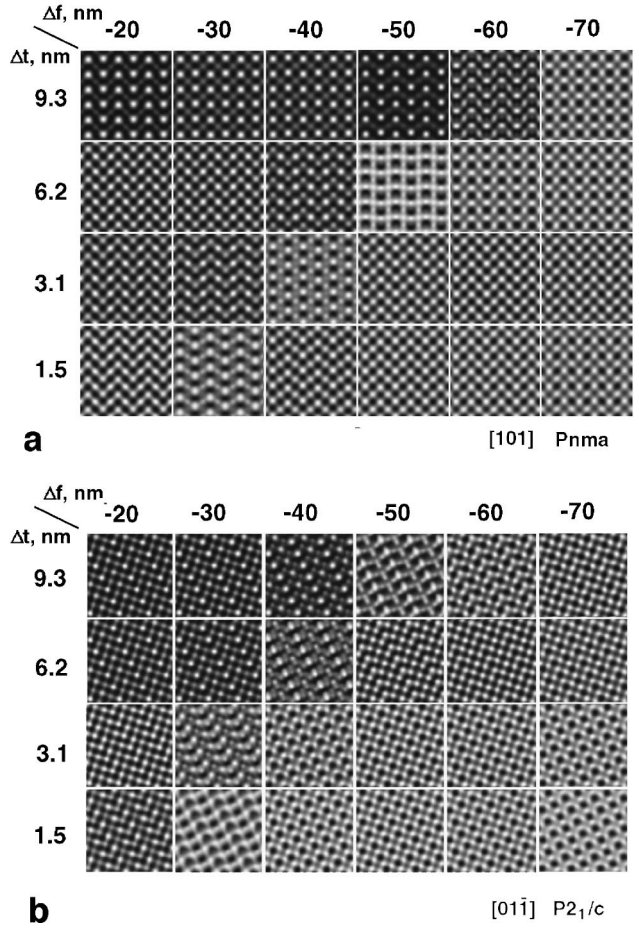

FIG. 11. Matrix of simulated images of the monoclinic structure of LCMO along the $[0\bar{1}1]_m$ zone. The specimen thickness was varied from 1.5 to 9.3 nm and the defocus is varied over the range -20 to -70 nm in steps of -10 nm.

monoclinic cell $P2_1/c$, is superposed on the experimental image.

''Period doubling,'' in the sense mentioned here, has been observed previously in a number of polytypic structures such as the ZnS-2H (wurtzite).[20] The two ZnS layers within a repeat period are structurally identical and related by symmetry. Nevertheless they are imaged as alternating rows of two different brightnesses, revealing in this way the true crystallographic period. In this simple case it could be shown that beam tilt produced this feature. The possibility that this would also apply to the present case could thus not be ruled out. However, image simulations of the orthorhombic *Pnma*-based structure under inclined beam incidence have failed to reproduce the period doubling. The same conclusion was reached in earlier work on isotypic manganates.[12] It was therefore concluded that, presumably, a structural difference between successive manganate layers, such as that occurring in the $P2_1/c$-based structure, could be responsible.

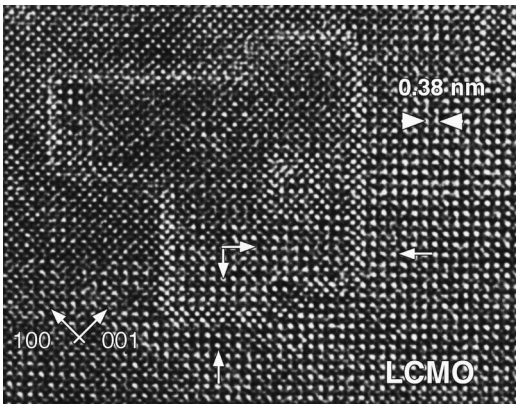

FIG. 12. Plan-view HREM image along $[010]_o$ of a free LCMO film. Note the presence of polygonal islands within which the dot pattern is in an antiphase relationship with respect to that in the surrounding matrix.

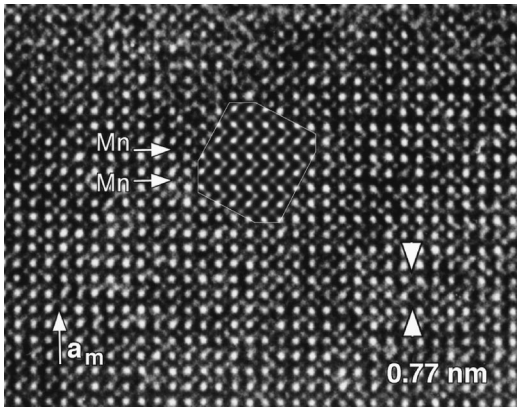

FIG. 13. HREM image of the ''doubling'' periodicity area of the film. The calculated image for defocus value $\Delta f = -20$ nm and thickness $t = 1.5$ nm is given as an inset.

The small monoclinic deformation also leads to an observable geometrical effect in the high-resolution images of cross-section specimens. The lattice of bright dots in Fig. 13 apparently looks square, but in actual fact the meshes are slightly deformed rectangles. The ''square'' meshes are slightly flattened in the $[010]_o \equiv [100]_m$ direction; moreover, the total lengths of the same large number of dot spacings measured along two mutually perpendicular diagonals of the ''square'' pattern are slightly different. These measurements suggest that in relatively small crystal blocks ($\sim$20 atom spacings) the structure is monoclinic.

Due to the domain fragmentation, as proved by the occurrence of composite diffraction patterns such as Fig. 5, the hypothetical monoclinic deformation is presumably a local feature and different in different domains, leading to a structure that is apparently orthorhombic in x-ray diffraction due to the averaging over domains.

2. Plan-view specimens

Plan-view images of specimens prepared with the substrate temperature at 890 °C exhibit a remarkably well-defined island pattern (Figs. 3 and 12). The straight interfaces, marked by bright lines or bright bands when seen edge on, are clearly parallel to $(101)_o$ and $(\bar{1}01)_o$ planes; except, they have small facets parallel to $(010)_m \equiv (100)_o$ planes. The interfaces have a certain width, marked by dots usually with a higher brightness than the bright dots within the domains and matrix as well. The density of bright dots along the boundary is, moreover, twice as large as that within or outside the island, the overall visual effect is a wide bright line. The geometry of the dot pattern within the islands is

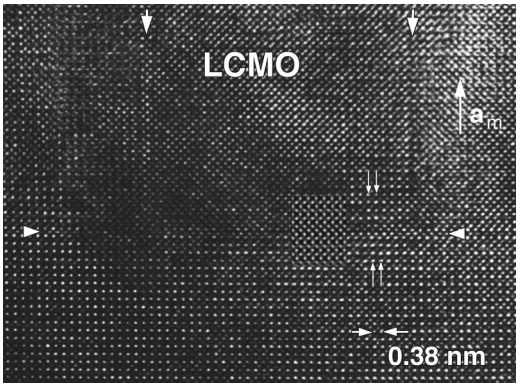

FIG. 14. Starting column limited by antiphase boundaries (upper part of the image). Period doubling along a_m is visible in the lower part of the image (matrix). The lattice of dots has a unit mesh that is a square slightly flattened along the a_m direction and is also slightly sheared in agreement with the monoclinic symmetry. A calculated image for a starting column is given as an inset.

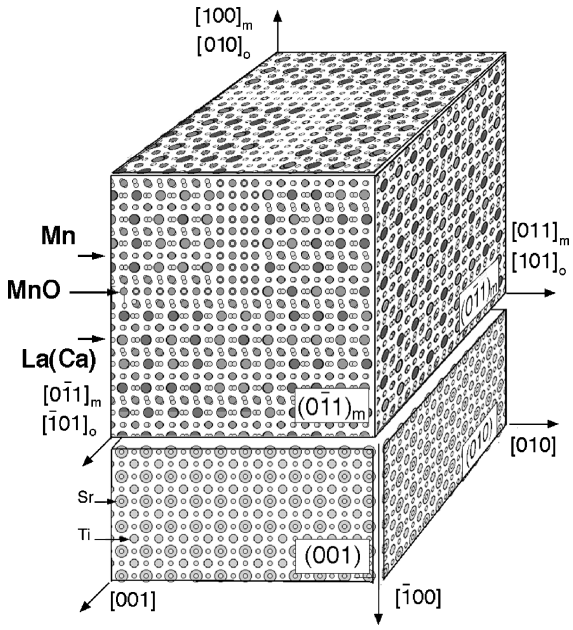

FIG. 15. Schematic spatial representation of antiphase domains in LCMO film.

often the same as that outside, but sometimes it is different, mainly in the intensity distribution not in the geometry of the dot pattern. However, it is clear that across the interfaces the brightest dot rows with a spacing of 0.54 nm in matrix and island are in all cases in antiphase relationship along both the $[101]_o$ and the $[\bar{1}01]_o$ directions, showing that the displacement vector of the interface is of the form $1/2[001]_m \equiv 1/2[100]_o$.

It is logical to assume that the closed polygonal antiphase boundaries in plan-view specimens, such as Fig. 12, are in fact cross sections of the columnar grains revealed in cross-section specimens. This interpretation is suggested by the good correlation between the average width of the columns in cross section and the average diameter of such polygons in plan view. Moreover, the separation lines between columns, imaged in Fig. 9, can be interpreted as edge on views of the planes in which such antiphase boundaries are situated (see Fig. 14).

In cross-section specimens most often no phase shift in the direction of the substrate normal b_o of the brightest dots row, parallel to the substrate plane, is visible. In a few cases such a shift is also observed in the edge region. A plausible model should account for these two possibilities as well as for the invariable presence of an antiphase shift in plan-view specimens. A model satisfying these requirements is based on the presence of a prismatically shaped antiphase boundary with a displacement vector of the type $1/2[100]_o \equiv 1/2[001]_m$. Prismatic columns that are completely embedded in the matrix do not give rise to a shift. Prismatic regions that, along the viewing direction, are not covered by matrix would exhibit such a shift. Moreover, the boundary model should be consistent with a realistic growth model leading to the observed features. This will be discussed in detail in a forthcoming paper.

V. DISCUSSION

The HREM images of the columnar structure shown in Fig. 9, can be interpreted in terms of two different models. As already mentioned above, symmetry considerations suggest that differently oriented domains can be formed along either the same or along different zone axes that are related by symmetry elements of the substrate surface. In particular, columnar domains, differing by a 90° rotation about the common $[010]_o$ zone are to be expected on these grounds. The difference in the HREM images of neighboring columns would then be due to the difference in orientation; one domain would, for instance, be imaged along a $[101]_o$ zone, whereas the adjacent one would be imaged along the $[\bar{1}01]_o$ zone. However, taking into account the quasitetragonal character of the structure, the images along $[101]_o$ and $[\bar{1}01]_o$ would not be drastically different under the same diffraction conditions and at the same thickness. Since in actual fact the images can be drastically different at all except at the smallest thickness, another more trivial explanation may be more probable. According to this model the difference in image characteristics between neighboring domains, in plan-view as well as in cross-section views, would be attributed to overlap of translation-related or perhaps even of rotation-related crystal blocks. The three-dimensional view of the column structure represented in Fig. 15 makes it clear that overlap of crystal blocks is likely to occur in plan-view as well as in cross-section views.

The disappearance of a difference in image along the thin edge of cross section specimens can be explained by the fact that in the thinnest areas overlap is unlikely to occur. Since the image in the overlap area depends not only on the assumed diffraction conditions but also on the level at which the antiphase boundary occurs (which is not known) and on its displacement vector, the number of parameters to be varied in order to obtain eventually correct correspondence between observed and simulated images becomes almost prohibitive. However, a clear indication that overlap is likely to be responsible for the observed two types of images was

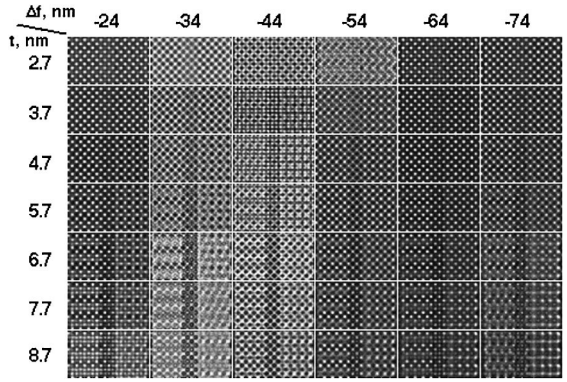

FIG. 16. Simulated images exhibiting the difference in dot pattern between the overlap part (left) and the nonoverlap part (right).

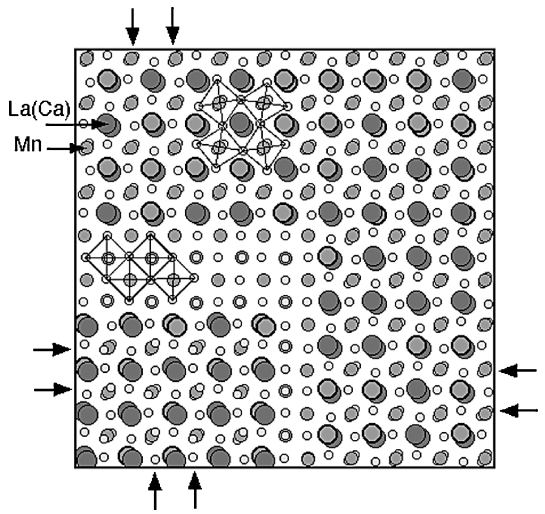

FIG. 17. Two-dimensional model used to simulate the image of a block of monoclinic LCMO containing an angular antiphase boundary. Along the viewing direction indicated by pairs of arrows, two blocks of crystal structure that are in an antiphase relationship overlap.

nevertheless obtained by simulating images (Fig. 16) The model of the crystal block is shown in Fig. 17. Overlap occurs along the two different directions (1) and (2) imaged in cross-section specimens, whereas the overlap in direction (3) is observed in plan-view specimens. The total thickness of the block along the viewing directions was varied from 2.7 to 8.7 nm in steps of 10 nm whereas the defocus was varied from -14 to -84 nm in steps of 10 nm. The antiphase boundary was assumed to be situated in the central plane and have a displacement vector of the type $\frac{1}{2}[110]_o$ or $\frac{1}{2}[011]_o$. The overlap part is represented in the left half of the frame and the matrix in the right part.

The simulated image obtained at $t \approx 5-7$ nm with a defocus $\Delta f \approx 20-30$ nm exhibits the main features of the observed images. This is in fact a rather critical test since under the same diffraction conditions and at the same thickness a pair of simulated images of two different structures has to match the observed pair of images.

The question should be raised why successive MnO_2 layers would have slightly different geometric configurations. A possible answer lies in the ability of Mn to adopt two different ionization states Mn^{3+} and Mn^{4+}. It is generally accepted that the substitution of Ca for La in $LaMnO_3$ leads to the transformation of part of the Mn^{3+} into Mn^{4+}. In the material studied approximately $\frac{1}{3}$ of the Mn would be in the 4+ state and $\frac{2}{3}$ in the 3+ state. The oxygen coordination octahedra associated with these differently charged ions may have different shapes; those associated with Mn^{3+} being subjected to a Jahn-Teller deformation, which produces a deformed MnO_6 octahedron. The elastic interaction between deformed octahedra may lead to a cooperative Jahn-Teller effect as a consequence of which layers of deformed octahedra may assemble along one of the ''cube'' planes of the basic perovskite structure in order to minimize the total free energy of elastic origin. Due to strain induced by the substrate one cubic plane may be favored over another, leading to the preferential ''doubling'' along the substrate normal.

According to the model of Fig. 15 the boundary is to be considered as a very thin lamella of rocksalt structure. Compounds with the rocksalt structure, especially those of transition elements, often contain a large concentration of vacancies. It is reasonable to assume that this is also the case in the MnO layers forming the boundary structure. This would explain why they always show up as strong bright lines as will be discussed more fully in a following paper.

VI. CONCLUSIONS

The presence in the electron diffraction patterns of spots that are not allowed by the spacegroup *Pnma*, as well as the observation of the corresponding period doubling along the substrate normal in high-resolution images, suggest that the space group of the basic structure of (La, Ca)MnO_3 might be monoclinic. Further investigations are desirable to confirm this. Moreover, the situation might be different in thin film and in bulk material.

The space group $P2_1/c$, which is a maximal subgroup of the *Pnma* space group, is consistent with a structure model that leads to computed images and diffraction patterns that are in agreement with the observations. The monoclinic model is compared with the orthorhombic model in Fig. 10.

The epitaxial films grown on STO exhibit a remarkable microtexture consisting of polyhedral columns parallel to the substrate normal separated by planar antiphase boundaries. In plan-view specimens these columns are revealed as closed polygonal domains. Very thin epitaxial films exhibit a microtexture consisting of separated islands. The microtexture may well play an important role in determining the magnitude of the colossal magnetoresistance effect observed in epitaxial films of manganites.

ACKNOWLEDGMENTS

O.I.L. is grateful to the Max-Planck Society (Germany) and DPWB (Belgium) for financial support during his stay. The authors are indebted to Dr. F. Phillipp and Dr. A. M. Abakumov for a helpful discussion. This work was performed within the framework of IUAP 4/10.

*Author to whom correspondence should be addressed.
[1] R. v. Helmholt, J. Wecker, B. Holzapfel, L. Schultz, and K. Samwer, Phys. Rev. Lett. **71**, 2331 (1993).
[2] K. Chahara, T. Ohno, M. Kasai, and Y. Kozono, Appl. Phys. Lett. **63**, 1990 (1993).
[3] H. L. Ju, C. Kwon, Q. Li, R. L. Greene, and T. Venkatesan, Appl. Phys. Lett. **65**, 2108 (1994).
[4] G. C. Xiong, Q. Li, H. L. Ju, S. N. Mao, L. Senapati, X. X. Xi, R. L. Greene, and T. Venkatesan, Appl. Phys. Lett. **66**, 1427 (1995).
[5] D. I. Khomskii and G. A. Sawatzky, Solid State Commun. **102**, 87 (1997).
[6] A. Maignan, Ch. Simon, V. Caignaert, and B. Raveau, C. R. Acad. Sci., Ser. I: Math. **321**, 297 (1995).
[7] H. L. Yakel, Jr., Acta Crystallogr. **8**, 394 (1955).
[8] G.-O. Gong, C. Canedy, G. Xiao, J. Z. Sun, A. Gupta, and W. J. Gallagher, Appl. Phys. Lett. **67**, 1783 (1995).
[9] E. O. Wollan and W. C. Koeher, Phys. Rev. **100**, 545 (1955).
[10] J. F. Mitchell, D. N. Argyrio, C. D. Potter, D. G. Hinks, J. D. Jorgensen, and S. D. Bader, Phys. Rev. B **54**, 6172 (1996).
[11] A. Maignan, C. Michel, M. Hervieu, and B. Raveau, Solid State Commun. **101**, 277 (1997).
[12] M. Hervieu, G. Van Tendeloo, V. Caignaert, A. Maignan, and B. Raveau, Phys. Rev. B **53**, 14 274 (1996).
[13] P. G. Radaelli, D. E. Cox, M. Marezio, S.-W. Cheong, P. E. Schiffer, and A. P. Ramirez, Phys. Rev. Lett. **75**, 4488 (1995).
[14] P. Dai, J. Zhang, H. A. Mook, S.-H. Liou, P. A. Dowben, and E. W. Plummer, Phys. Rev. B **54**, R3694 (1996).
[15] G. Zhao, K. Conder, H. Keller, and K. A. Muller, Nature (London) **381**, 676 (1996).
[16] S. Jin, M. McCormack, T. H. Tiefel, and R. Ramesh, J. Appl. Phys. **76**, 6929 (1994).
[17] J. O'Donnel, M. Onellion, M. S. Rzchowski, J. N. Eckstein, and I. Bozovic, Phys. Rev. B **54**, R6841 (1996).
[18] E. Gommert, H. Cerva, A. Rucki, R. v. Helmolt, J. Wecker, C. Kuhrt, and K. Samwer, J. Appl. Phys. **81**, 5496 (1997).
[19] H.-U. Habermeier, Eur. J. Solid State Inorg. Chem. **28**, 201 (1991).
[20] W. Coene, H. Bender, F. C. Lovey, D. van Dyck, and S. Amelinckx, Phys. Status Solidi A **87**, 483 (1985).